J. Fluid Mech. (2021), *vol*. 915, A19, doi:10.1017/jfm.2021.97

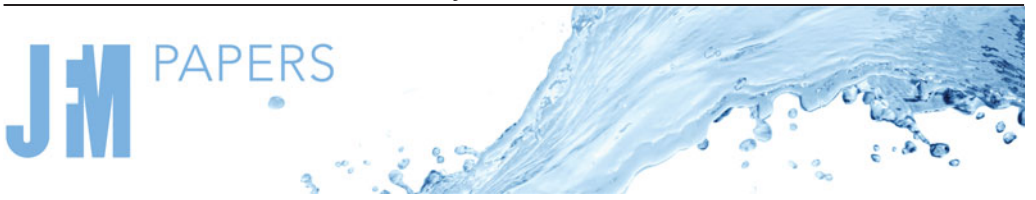

Surface wave pattern formation in a cylindrical container

X. Shao[1], P. Wilson[1], J.R. Saylor[1] and J.B. Bostwick[1],†

[1]Department of Mechanical Engineering, Clemson University, Clemson, SC 29634, USA

(Received 16 July 2020; revised 8 January 2021; accepted 25 January 2021)

Surface waves are excited by mechanical vibration of a cylindrical container having an air/water interface pinned at the rim, and the dynamics of pattern formation is analysed from both an experimental and theoretical perspective. The wave conforms to the geometry of the container and its spatial structure is described by the mode number pair (n, ℓ) that is identified by long exposure time white light imaging. A laser light system is used to detect the surface wave frequency, which exhibits either a (i) harmonic response for low driving amplitude edge waves or (ii) sub-harmonic response for driving amplitude above the Faraday wave threshold. The first 50 resonant modes are discovered. Control of the meniscus geometry is used to great effect. Specifically, when flat, edge waves are suppressed and only Faraday waves are observed. For a concave meniscus, edge waves are observed and, at higher amplitudes, Faraday waves appear as well, leading to complicated mode mixing. Theoretical predictions for the natural frequency of surface oscillations for an inviscid liquid in a cylindrical container with a pinned contact line are made using the Rayleigh–Ritz procedure and are in excellent agreement with experimental results.

Key words: Faraday waves, parametric instability, pattern formation

1. Introduction

Pattern formation on liquid interfaces is used in industrial applications like spray cooling (Kim 2007) and biomedical technologies such as drop atomization for drug delivery (James *et al.* 2003; Vukasinovic, Smith & Glezer 2007; Tsai *et al.* 2014), and has recently been shown to facilitate the assembly of particles on the microscale (Chen *et al.* 2014), which includes organoid cells (Chen *et al.* 2015) that are used in tissue engineering applications (Guven *et al.* 2015). Often, modern bioprinting technologies require precise spatial and temporal control of surface patterns in liquids confined to small containers, such that container geometry determines the wave symmetry, and that is our focus. In this paper, we characterize the surface wave dynamics of a cylindrical container with

† Email address for correspondence: jbostwi@clemson.edu

two meniscus configurations that is mechanically vibrated and report the first 50 pure resonance modes, as well as more complicated spatial patterns that involve the mixing of two waves with completely different dynamics.

Faraday waves are synonymous with pattern formation and have been widely studied for their ability to, e.g. redistribute particles (Wright & Saylor 2003; Saylor & Kinard 2005) and surfactants (Strickland, Shearer & Daniels 2015) on thin liquid films, rearrange layers of granular media (Melo, Umbanhowar & Swinney 1994), and induce turbulent mixing of two miscible fluids (Briard, Gostiaux & Gréa 2020). This canonical problem in fluid mechanics was first studied by Faraday (1831), who showed the interface of a vertically vibrated liquid bath will lose stability to standing surface waves, which oscillate at half the driving frequency. This is termed a sub-harmonic response and is characteristic of parametric oscillations. Benjamin & Ursell (1954) used a linear stability analysis to show that Faraday waves obey a Mathieu equation for the dynamics, with standing waves appearing inside the 'tongues of instability' in the driving frequency–amplitude space. Here, the wave frequency can be sub-harmonic (half the driving frequency), harmonic (equal to the driving frequency), or super-harmonic (integer multiples of the driving frequency). Most studies of Faraday waves report a sub-harmonic response as this instability tongue typically has the lowest onset acceleration, but there are exceptions such as the case of thin viscous fluid layers where the harmonic instability tongue has lower onset acceleration than the sub-harmonic one (Kumar 1996; Müller *et al.* 1997). Complex quasi-patterns can be observed when there are multiple driving frequencies present (Edwards & Fauve 1994; Batson, Zoueshtiagh & Narayanan 2015). For references to the vast literature, see the review articles by Miles & Henderson (1990) and Perlin & Schultz (2000).

The presence of a meniscus at the contact line between the interface and vibrating container induces motions that are harmonic with respect to the driving frequency and are referred to as edge waves. These typically appear for driving amplitudes much lower than the Faraday wave threshold and researchers often try to suppress such waves by using large aspect ratio (relative to the wavelength) containers (Christiansen, Alstrøm & Levinsen 1995), using high concentrations of soluble surfactants to enable an unpinned, sliding, meniscus (Henderson & Miles 1990, 1991), or by using a highly viscous fluid such that the edge waves are quickly damped (Bechhoefer *et al.* 1995). In general, for high driving frequencies, the spatial wavenumber is continuous and the edge conditions and/or container geometry do not affect Faraday waves, as shown by Edwards & Fauve (1994) for some irregular container geometries. Notably, Ghadiri & Krechetnikov (2019) have studied Faraday waves in time-dependent domains, revealing a number of new dynamics, including a secondary Eckhaus instability of the primary wave pattern.

For small containers, surface waves conform to the container geometry, as shown by Douady & Fauve (1988) and Douady (1990). In this case, the allowable surface modes have large wavelength, exhibit a discrete mode number pair determined by the container geometry, and have a finite bandwidth over which that particular mode can be excited, as shown by Henderson & Miles (1990) in a cylindrical container. Notably, the natural frequencies and decay rates for surface waves in a brimful cylindrical container have been experimentally measured by Henderson & Miles (1994). Ciliberto & Gollub (1984, 1985) have shown that, in finite-size cylindrical containers, two modes that share nearly the same frequency may interact and give rise to chaotic dynamics (Gluckman *et al.* 1993). Contact-line conditions become particularly important for low mode number shapes because dissipation from contact-line motion (Davis 1980; Hocking 1987; Bostwick & Steen 2015) can be comparable to bulk viscous dissipation and this can affect the

threshold acceleration. To eliminate contact-line dissipation, one can either create a pinned contact line or a free-sliding contact line by either using surfactants (Henderson & Miles 1990) or two or more carefully chosen immiscible liquids (Batson, Zoueshtiagh & Narayanan 2013; Ward, Zoueshtiagh & Narayanan 2019). The advantage of the free-sliding contact-line condition is that it can be compared to the theory of Kumar & Tuckerman (1994). In our experiments, we use a pinned contact-line condition and carefully control the meniscus geometry to either (i) suppress edge waves to study the onset of pure Faraday waves or (ii) purposefully excite edge waves to observe complex mode mixing phenomena.

Theoretical modelling and analysis of surface waves in containers with pinned contact lines (as created in experiment by filling a tank until the meniscus is pinned at the tank rim) are not as straightforward to analyse as the free-sliding contact-line case. This is because the pinned contact-line condition is incompatible with the no-penetration condition at the container sidewall, which makes it impossible to factor a spatial normal mode through the governing equations to deliver a purely time-dependent evolution equation from which the dispersion relationship can be obtained. This makes the problem over constrained. In contrast, the free contact line is the natural boundary condition, i.e. compatible with the no-penetration condition, making the analysis more straightforward, as shown in the derivation of the Mathieu equation by Benjamin & Ursell (1954). New analytical techniques have been developed to address the pinned contact line including using a variational approach with Lagrange multiplier (Benjamin & Scott 1979; Graham-Eagle 1983), introducing a singular pressure (contact force) at the contact line (Prosperetti 2012), or using a Rayleigh–Ritz variational procedure over a constrained function space (Bostwick & Steen 2009). With regard to cylindrical containers with pinned contact lines, viscous dissipation has been theoretically considered by Henderson & Miles (1994) for the first-order approximation within the Stokes boundary layer and was later extended to higher-order approximations by Martel, Nicolas & Vega (1998). Miles & Henderson (1998) further consider the added effect of viscous dissipation within the bulk liquid and how this affects the decay rate. The theoretical development we present here uses the Rayleigh–Ritz approach which shows excellent agreement between the predicted resonance frequencies and experimental observations of our mode catalogue.

We begin this paper by describing the experimental set-up and techniques to determine the spatial wave structure and associated dynamics in § 2. Experimental results are reported in § 3 where we present the observation of the first 50 resonant modes, contrast the dynamic response of harmonic edge waves from sub-harmonic Faraday waves, and reveal complex mode mixing phenomena of edges waves with Faraday waves at a fixed driving frequency. In § 4, we develop a theoretical model to predict the frequency and surface mode shapes of an inviscid fluid in a cylindrical container with pinned contact line. Comparisons between theoretical predictions and experimental observations are made and show excellent agreement. Lastly, we offer some concluding remarks in § 5.

2. Experiment

Surface waves are excited in the experimental set-up shown in figure 1(*a*). A circular Plexiglass tank of radius $R = 35$ mm and height $H = 22$ mm is mounted on a Labworks ET-139 electromechanical shaker which provides vertical vibration of the tank. The shaker is driven by an Agilent 33220A function generator and Labworks PA-141 amplifier combination over a range of driving frequencies $f_d = 7$–47 Hz. The tank acceleration a was measured using a PCB 352C33 accelerometer and a PCB 482C05 signal

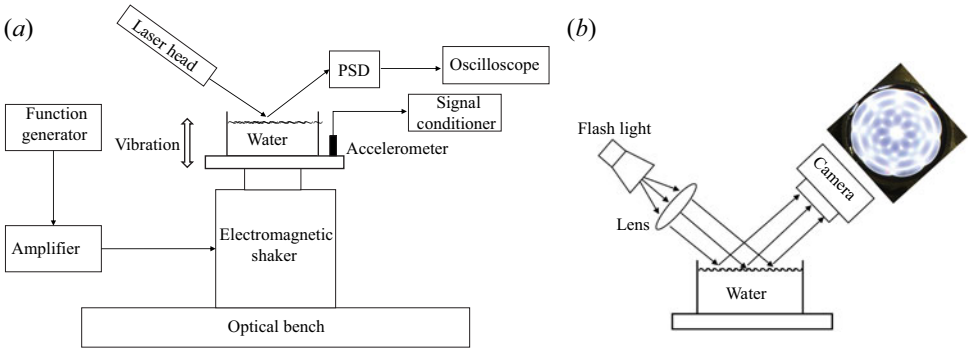

Figure 1. Schematic diagrams of (*a*) overall experimental set-up and (*b*) imaging system.

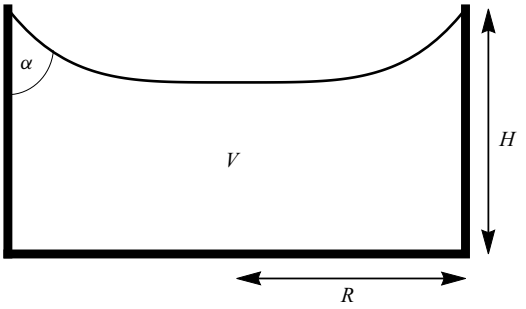

Figure 2. Schematic of meniscus geometry illustrating the contact angle α formed by a volume of water V that creates a pinned contact line at the rim of the cylindrical container.

conditioner combination. Herein, we define the acceleration amplitude as A, which is the average min–max of a.

The tank is filled to the brim with a volume V of deionized water such that the contact line is pinned and there are no dynamic contact-line effects. This creates a meniscus with contact angle α that can be controlled by subsequently adding or removing fluid from the container so that $\alpha < 90^\circ$ (underfilling) or $\alpha > 90^\circ$ (overfilling). The contact angle is illustrated in figure 2 and will be further discussed shortly. The scaled volume $\hat{V} \equiv V/\pi R^2 H$ could also be used to determine the degree of under-filling $\hat{V} < 1$ or over-filling $\hat{V} > 1$. The relevant material properties for doubly deionized water used in these experiments are the density $\rho = 997\ \mathrm{kg\,m^{-3}}$, dynamic viscosity $\mu = 10^{-3}$ Pa s and surface tension $\sigma = 72\ \mathrm{mN\,m^{-1}}$. For capillary motions, there are two relevant time scales; the viscous time scale $t_v = \mu R/\sigma$ and inertial time scale $t_c = \sqrt{\rho R^3/\sigma}$, with the relative balance given by the Ohnesorge number $Oh \equiv \mu/\sqrt{\rho R\sigma} = 6 \times 10^{-4}$, which for our experiment displays inviscid motions. The Bond number is $Bo \equiv \rho g R^2/\sigma = 167$ where g is the gravitational acceleration.

A laser light system is used to measure the surface wave frequency and detect the onset acceleration of Faraday waves, as shown in figure 1(*a*). A helium–neon laser beam (632.8 nm wavelength) is incident on the free surface and reflected to a position sensitive detector, which gives an analog voltage output proportional to the position of the centroid of the light striking the sensor. The output signal is transmitted to an oscilloscope and processed through a fast Fourier transform (FFT) operation, which gives the surface wave frequency. For Faraday waves, the observed frequency f_o is half the driving frequency $f_o = 0.5 f_d$.

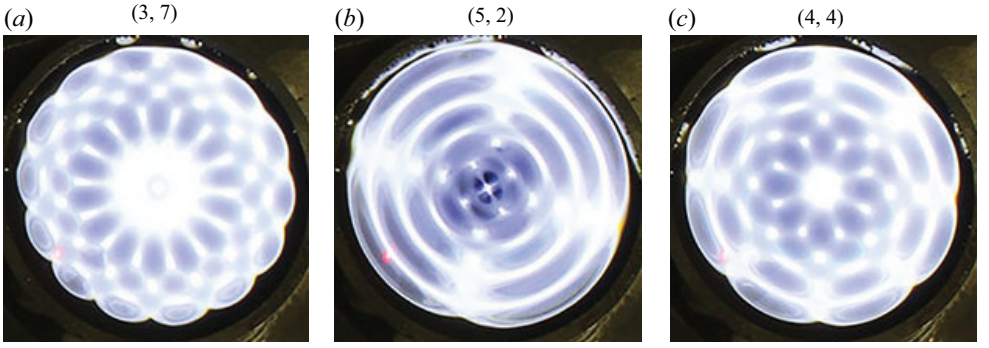

Figure 3. Typical experimentally observed Faraday wave modes with mode number pair (n, ℓ).

In our experiment, for small forcing amplitude the measured wave frequency is identical to the driving frequency $f_o = f_d$ whenever $\alpha \neq 90^\circ$, which is indicative of edge waves excited from the sidewall of the container. This is a geometric effect and not related to dynamic contact-line motion. For fixed driving frequency f_d, the Faraday wave threshold is approached by increasing the tank acceleration until we observe the rapid growth of a frequency peak with $f_o = 0.5 f_d$ on the FFT. The corresponding acceleration A_u is the upper limit of the threshold acceleration for that driving frequency. The amplitude is then decreased until that frequency peak disappears on the FFT and we define this as the lower limit of the threshold acceleration A_l. The threshold acceleration lies between A_u and A_l. Several iterations are successively performed until the difference between A_u and A_l is smaller than 0.2 $\mathrm{m\,s^{-2}}$. We then report the experimental threshold acceleration as the average value $A = (A_u + A_l)/2$.

The surface wave structure is characterized by the optical system shown in figure 1(*b*). Collimated light is produced by a lens located one focal length $f = 300$ mm from a white light source. To improve the degree of collimation a plate with a 2 mm diameter hole was placed in front of the light source. The collimated beam is directed at the wave surface and the reflected light captured by a digital camera (Canon EOS Rebel T3i) with a Canon EF-S 18–55 mm lens. A long exposure time 0.6 s is set for most of the images presented herein in order to blur out the travelling edge waves originating from the container sidewall and highlight the standing wave pattern. The exception being the lowest frequencies explored where the exposure time was set to 0.8 s to ensure that travelling waves were truly blurred out. In this way, the dominant wave pattern in the imagery is either edge waves under resonant conditions, or Faraday waves, or both. Edge waves away from resonance condition will become blurred and have more uniform light intensity. The optical axis of the camera is oriented normal to the reflected light such that locations where the wave slope is zero (i.e. the peak or trough) are bright, whereas the regions where the wave slope is non-zero (i.e. the nodes) appear dark. Larger slopes lead to darker regions. Typical wave patterns are shown in figure 3. To identify the modal structure, we compute the two-dimensional (2-D) cross-correlation between the experimental wave pattern and the Bessel function $\mathrm{J}_\ell(k_n r)\cos(\ell\theta)$, defined in cylindrical coordinates (r, θ), where ℓ is the azimuthal mode number and k_n is computed from the roots of $\mathrm{J}'_\ell(k_n R) = 0$ (n is the numerical order of those roots). This generates a table of 2-D cross-correlations in the (n, ℓ) mode number space. Because of the existence of phase difference in the azimuthal direction between the experimental and target images, we rotate the target image 360° about its centre and identify the maximum value of the 2-D cross-correlation. We repeat this procedure for all target modes in the table and identify the maximum value of

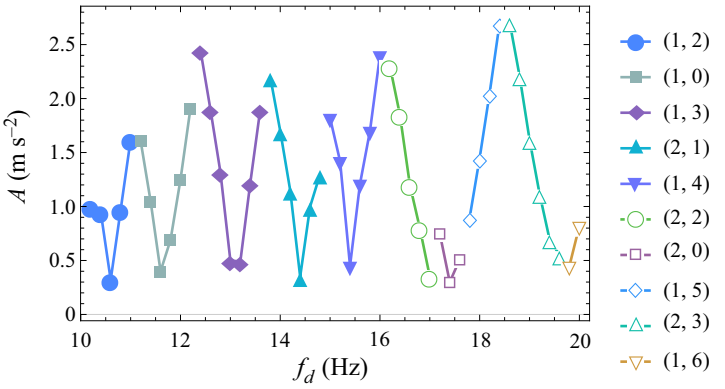

Figure 4. Acceleration A against driving frequency f_d showing the Faraday wave tongues for various modes (n, ℓ).

the 2-D cross-correlation, which we associate with the modal structure of the experimental image. This procedure has been done for the images shown in figure 3, yielding mode number pairs (3, 7), (5, 2), (4, 4), respectively. We note that the 2-D cross-correlations can be improved by using the predicted surface shapes that we present later in our theoretical development. However, this does not change the modal identification of our experimental results. Lastly, we mention that this technique breaks down when the surface wave is a superposition of harmonic edge waves and sub-harmonic Faraday waves, as will be discussed in § 4.

3. Experimental results

We report a number of experimental observations and these generally depend upon the magnitude of the driving amplitude. High-amplitude forcing above the Faraday wave threshold produces sub-harmonic waves, while low-amplitude forcing below threshold leads to harmonic edge waves under the proper experimental protocol. In some circumstances it is possible to simultaneously excite both a sub-harmonic wave and harmonic wave with different modal structures for the same driving frequency. We call these mixed modes. We note in passing that it is possible to generate Faraday waves that are harmonic, however, the conditions under which these occur are not explored in this work.

3.1. *Faraday waves*

To suppress harmonic edge waves in these experiments, we fill the container such that the contact angle $\alpha = 90^\circ$. This serves to eliminate edge waves, leaving the interface perfectly flat at accelerations below the Faraday wave threshold. A frequency sweep is performed using an interval of 0.2 Hz and the threshold acceleration is determined for each frequency, following the procedure described above, giving the results shown in figure 4. For a fixed frequency, the interface is flat below the threshold acceleration which becomes the oscillating surface shape defined by (n, ℓ) above threshold. A given mode (n, ℓ) can be excited over a range of frequencies and the particular frequency with the lowest threshold acceleration is twice the resonance frequency for that particular mode. Note that the onset acceleration at resonance is relatively constant for all modes. Typical Faraday wave tongues are shown in figure 4 for the (1, 0), (1, 2), (1, 3), (2, 1), (1, 4) modes. For the other modes,

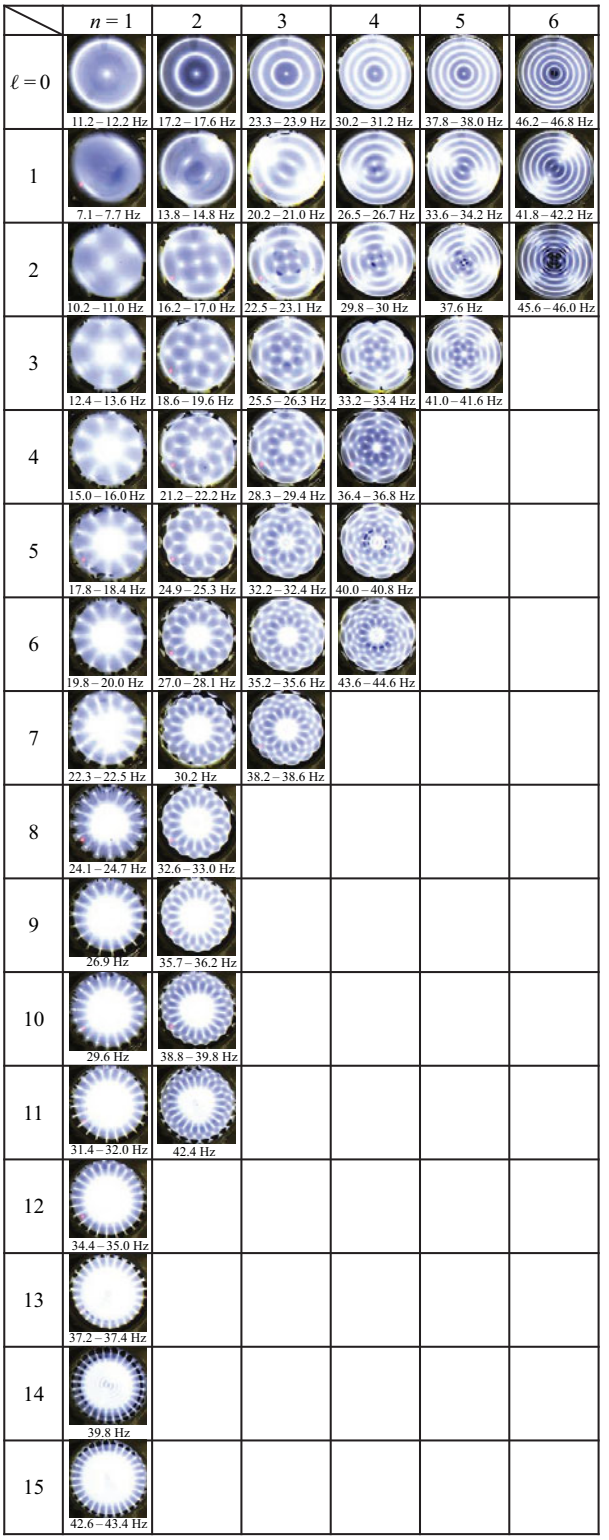

Figure 5. Experimentally observed Faraday wave mode shapes defined by the mode number pair (n, ℓ) with corresponding driving frequency range.

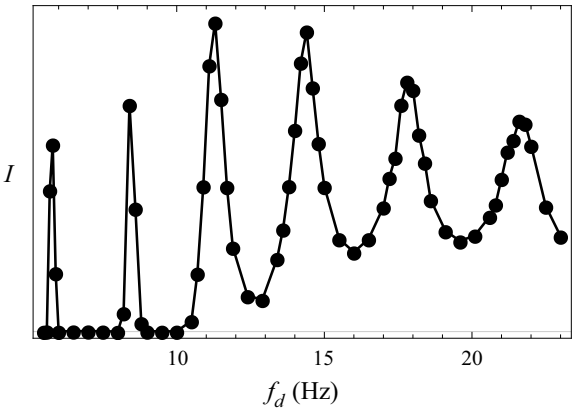

Figure 6. Edge wave frequency response plotting a measure of the light intensity I against the driving frequency f_d.

e.g. the (2, 2) or (1, 5) modes, we can only obtain the left-hand side or right-hand side of the instability tongue, respectively. In these situations, we take the resonance frequency to be the frequency at the smallest acceleration. This is likely due to the overlap of instability tongues or mode competition in these frequency ranges, where the tongues are clustered close together. Furthermore, some modes, e.g. the (1, 6) mode, can only be excited over a small frequency window which makes it challenging to experimentally observe. Despite this fact, we have experimentally observed the first 50 Faraday wave modes, as shown in figure 5 with the corresponding driving frequency range. Those difficult to find modes have been discovered with the aid of theoretical predictions that we develop in a forthcoming section.

3.2. *Edge waves*

Harmonic edge waves can be excited by under-filling the container such that $\alpha < 90^\circ$ wherein edge waves occur for driving amplitudes much smaller than the Faraday wave threshold. Edge waves are always axisymmetric $\ell = 0$ and the radial mode number n increases with frequency. Figure 6 shows the frequency response for edge waves with a driving amplitude below the Faraday wave threshold. Here, we plot a measure of the light intensity against the driving frequency. As noted above, away from resonance, travelling waves are observed and are blurred in the imagery due to the long exposure time of the images. This is shown in figure 7(*a–e*), which shows the image of the $n = 5$ mode as the frequency is increased from just below resonance to just above resonance. The frequency response exhibits 6 resonance peaks within this range of driving frequencies, images of which are shown in figure 7(*f–j*). The first peak corresponds to the (1, 0) mode, the second peak to the (2, 0) mode and so on. Note that the bandwidth for a given mode increases with frequency and mode number n, e.g. the (6, 0) mode has a larger bandwidth than the (1, 0) mode, and this is consistent with increased dissipation for higher mode numbers, even though the viscosity of water is small (Bostwick & Steen 2016).

3.3. *Mode mixing*

By increasing the driving amplitude above the Faraday wave threshold, we have observed the simultaneous excitation of harmonic edge waves with sub-harmonic Faraday waves

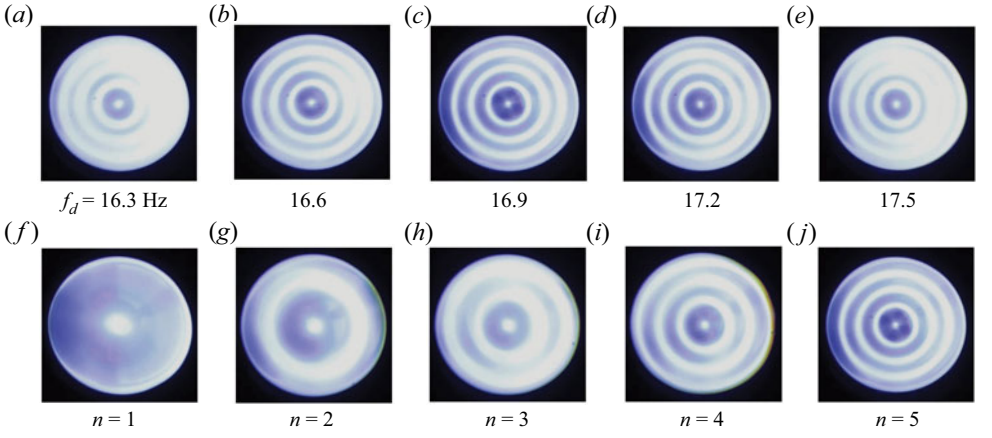

Figure 7. Edge waves (*a–e*) for driving frequencies $f_d = 16.3$ to 17.5 Hz show the images becoming progressively less clear away from resonance at 16.9 Hz for the $n = 5$ mode and (*f–j*) corresponding resonant modes for $n = 1, 2, 3, 4, 5$.

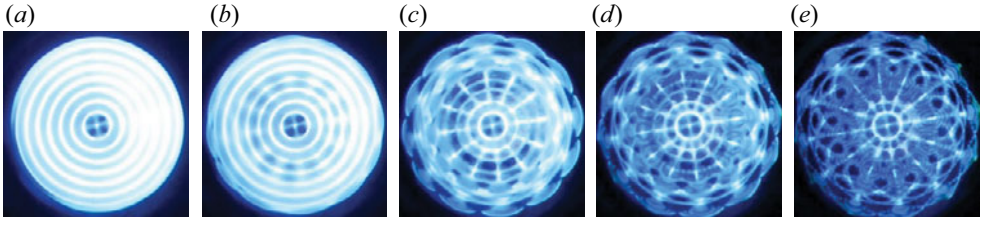

Figure 8. Mode mixing is observed upon increasing the driving amplitude from (*a*) to (*e*) for driving frequency $f_d = 34.7$ Hz. A pure harmonic edge wave (*a*,*b*) mixes with a sub-harmonic azimuthal wave above the threshold acceleration (*c*). Further increasing the driving amplitude leads to a high-amplitude mixed mode (*d*,*e*).

when the tank is under-filled ($\alpha < 90^\circ$). Here, an axisymmetric $(n, 0)$ edge wave mixes with an azimuthal (n, ℓ) Faraday wave leading to a complex, beautiful, spatial pattern. Figure 8 shows a typical amplitude sweep for fixed driving frequency $f_d = 34.7$ Hz. For small driving amplitude, harmonic edge waves are excited (*a*) and once the threshold acceleration is reached (*b*) a sub-harmonic Faraday wave is born that evolves into a steady wave pattern (*c*). Incremental increases in driving amplitude above threshold result in high-amplitude patterns (*d*,*e*). We note that unsteady Faraday waves were observed beyond the forcing amplitudes explored here, but we did not pursue these motions further. Figure 9 shows a number of mixed modes with the corresponding driving frequency. The edge wave frequency response diagram in figure 6 and mode table in figure 5 can be used to identify the corresponding mixing modes at the particular driving frequency. For example, the $f_d = 13.4$ Hz image in figure 9 is the superposition of the $(4, 0)$ harmonic edge wave and $(1, 3)$ sub-harmonic Faraday wave. Because these motions are observed deep into the instability tongue, it is possible they are susceptible to nonlinear effects such as mode–mode interactions but we do not pursue this further.

4. Theory of surface waves in a cylindrical container

Consider a cylindrical container of radius R and height H filled with an inviscid fluid that creates a pinned contact line in cylindrical coordinates (r, θ, z), as shown in figure 10. The flat interface has surface tension σ and is given a small disturbance $\xi(r, \theta, t)$. In what

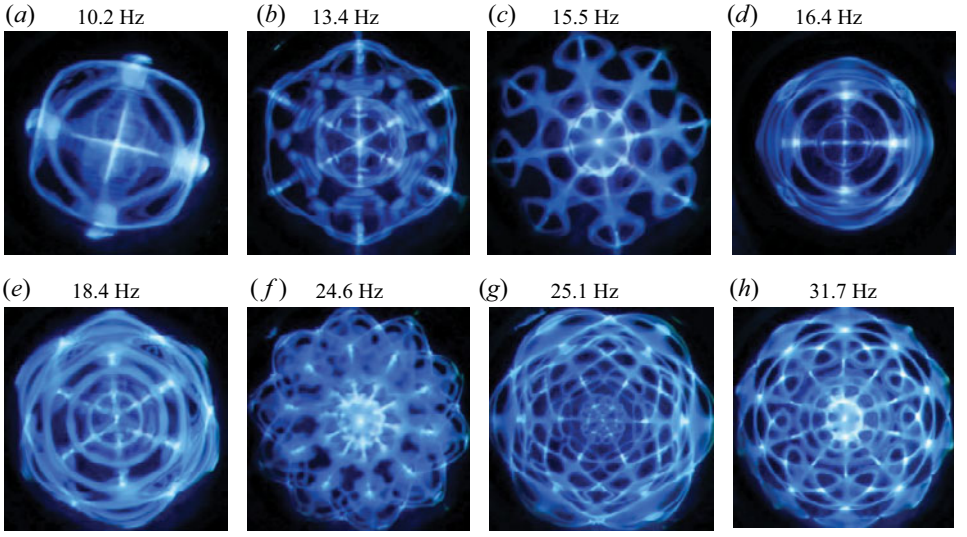

Figure 9. High-amplitude mixed modes are observed at the indicated driving frequency.

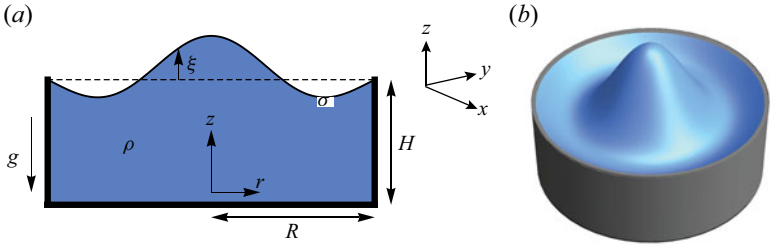

Figure 10. Definition sketch in (*a*) 2-D planar and (*b*) 3-D perspective views.

follows we perform a linear stability analysis, wherein the pressure p and velocity fields $\boldsymbol{v}$ will be associated with the disturbance fields.

4.1. *Hydrodynamic field equations*

The fluid is assumed to be incompressible and the flow irrotational, which allows us to define the velocity fields as $\boldsymbol{v} = \nabla\Phi$, where the velocity potential Φ satisfies Laplace's equation

$$\nabla^2\Phi = 0. \tag{4.1}$$

The velocity potential satisfies the no-penetration condition

$$\left.\frac{\partial\Phi}{\partial r}\right|_{r=R} = 0, \quad \left.\frac{\partial\Phi}{\partial z}\right|_{z=0} = 0, \tag{4.2a,b}$$

at the walls of the cylindrical container and a kinematic condition

$$\frac{\partial\Phi}{\partial z} = \frac{\partial\xi}{\partial t} \tag{4.3}$$

on the free surface $z = H$, which relates the normal velocity to the perturbation amplitude there. The pressure field in D for small interface disturbance is given by the linearized

Bernoulli equation

$$p = -\rho \frac{\partial \Phi}{\partial t} - \rho g \xi, \tag{4.4}$$

where ρ is the fluid density and g is the gravitational constant. The pressure at the free surface is governed by the linearized Young–Laplace equation

$$\frac{p}{\sigma} = -\frac{1}{R^2}\left(\frac{\partial^2 \xi}{\partial r^2} + \frac{1}{r}\frac{\partial \xi}{\partial r} + \frac{1}{r^2}\frac{\partial^2 \xi}{\partial \theta^2}\right), \tag{4.5}$$

valid for small disturbances $|\xi| \ll 1$. The pinned contact-line condition is given by

$$\xi|_{r=R} = 0. \tag{4.6}$$

Lastly, volume conservation is enforced by the integral condition

$$\int_0^{2\pi}\int_0^R r\xi(r,\theta)\,\mathrm{d}r\,\mathrm{d}\theta = 0. \tag{4.7}$$

Equations (4.1)–(4.7) are the linearized disturbance equations which are a well-posed system of partial differential equations.

4.2. *Normal modes*

The following dimensionless variables are introduced:

$$\bar{r} = r/R, \quad \bar{z} = z/R, \quad \bar{\xi} = \xi/R, \quad \bar{t} = t\sqrt{\frac{\sigma}{\varrho r^3}}, \quad \bar{\Phi} = \Phi\sqrt{\frac{\rho}{\sigma R}}, \quad \bar{p} = p\left(\frac{R}{\sigma}\right). \tag{4.8a–f}$$

Here, lengths are scaled by the radius of the cylinder R, time with the capillary time scale $\sqrt{\rho R^3/\sigma}$ and pressure with the capillary pressure σ/R.

Normal modes,

$$\Phi(\boldsymbol{x}, t) = \phi(r, z)\mathrm{e}^{\mathrm{i}\omega t}\mathrm{e}^{\mathrm{i}\ell\theta}, \quad \xi(r, \theta, t) = y(r)\mathrm{e}^{\mathrm{i}\omega t}\mathrm{e}^{\mathrm{i}\ell\theta}, \tag{4.9a,b}$$

are then applied with the scalings (4.8*a–f*) to the domain equations to yield

$$\frac{1}{r}\frac{\partial}{\partial r}\left(r\frac{\partial \phi}{\partial r}\right) - \frac{\ell^2}{r^2}\phi + \frac{\partial^2 \phi}{\partial z^2} = 0, \quad p = -\mathrm{i}\lambda\phi - Bo\, y, \tag{4.10}$$

with corresponding boundary conditions

$$\left.\frac{\partial \phi}{\partial r}\right|_{r=1} = 0, \quad \left.\frac{\partial \phi}{\partial z}\right|_{z=0} = 0, \quad p|_{z=h} = -\left(\frac{\partial^2 y}{\partial r^2} + \frac{1}{r}\frac{\partial y}{\partial r} - \frac{\ell^2}{r^2}y\right),$$
$$\left.\frac{\partial \phi}{\partial z}\right|_{z=h} = \mathrm{i}\lambda y, \quad y|_{r=1} = 0. \tag{4.11a–e}$$

Here, $\lambda \equiv \omega\sqrt{\rho R^3/\sigma}$ is the scaled frequency, $h = H/R$ the cylinder aspect ratio and $Bo \equiv \rho g R^2/\sigma$ the Bond number. The volume conservation constraint (4.7) is naturally satisfied for $\ell \neq 0$, but for $\ell = 0$ requires

$$\int_0^1 r y(r)\,\mathrm{d}r = 0. \tag{4.12}$$

4.3. *Integro-differential equation*

This is an interfacial-driven flow and we can derive a single integro-differential equation for the interface disturbance y by mapping the problem to the interface. This is a boundary integral approach. To begin, a Bessel series solution for ϕ is sought,

$$\phi(r, z) = \sum_{n=1}^{\infty} A_n \cosh(k_{n\ell} z) \mathrm{J}_\ell(k_{n\ell} r), \tag{4.13}$$

where $k_{n\ell}$ is the nth zero of $\mathrm{J}'_\ell(k)$, as required to satisfy the no-penetration condition at the lateral sidewall ($r = 1$), with J_ℓ the Bessel function. Note that the no-penetration condition at the bottom of the container $z = 0$ is naturally satisfied by this solution. Similarly, the interface disturbance y can be expanded as

$$y(r) = \sum_{n=1}^{\infty} C_n \mathrm{J}_\ell(k_{n\ell} r), \quad C_n = \frac{\langle y, \mathrm{J}_\ell(k_{n\ell} r)\rangle}{\langle \mathrm{J}_\ell(k_{n\ell} r), \mathrm{J}_\ell(k_{n\ell} r)\rangle}, \tag{4.14a,b}$$

where the inner product is defined as

$$\langle f(r), g(r)\rangle = \int_0^1 r f(r) g(r)\, \mathrm{d}r. \tag{4.15}$$

The coefficients A_n, C_n are related by the kinematic condition, $A_n = \mathrm{i}\lambda C_n / k_{n\ell} \sinh(k_{n\ell} h)$, and this gives the general solution for the velocity potential

$$\phi(r, z) = \mathrm{i}\lambda \sum_{n=1}^{\infty} \frac{1}{k_{n\ell}} \frac{\cosh(k_{n\ell} z)}{\sinh(k_{n\ell} h)} \frac{\langle y, \mathrm{J}_\ell(k_{n\ell} r)\rangle}{\langle \mathrm{J}_\ell(k_{n\ell} r), \mathrm{J}_\ell(k_{n\ell} r)\rangle} \mathrm{J}_\ell(k_{n\ell} r), \tag{4.16}$$

written implicitly through y. This solution is applied to the Young–Laplace equation to give

$$\lambda^2 \sum_{n=1}^{\infty} \frac{\coth(k_{n\ell} h)}{k_{n\ell}} \frac{\langle y, \mathrm{J}_\ell(k_{n\ell} r)\rangle}{\langle \mathrm{J}_\ell(k_{n\ell} r), \mathrm{J}_\ell(k_{n\ell} r)\rangle} \mathrm{J}_\ell(k_{n\ell} r) - Bo\, y + \left[\frac{\mathrm{d}^2 y}{\mathrm{d}r^2} + \frac{1}{r}\frac{\mathrm{d}y}{\mathrm{d}r} - \frac{\ell^2}{r^2} y\right] = 0, \tag{4.17}$$

which is an integro-differential equation for the interface disturbance y.

4.4. *Operator formalism*

The governing integro-differential eigenvalue problem (4.17) can be recast as an operator equation

$$\lambda^2 M[y] + K[y; Bo] = 0, \tag{4.18}$$

with

$$M[y] \equiv \sum_{n=1}^{\infty} \frac{1}{k_{n\ell}} \coth(k_{n\ell} h) \frac{\langle y, \mathrm{J}_\ell(k_{n\ell} r)\rangle}{\langle \mathrm{J}_\ell(k_{n\ell} r), \mathrm{J}_\ell(k_{n\ell} r)\rangle} \mathrm{J}_\ell(k_{n\ell} r), \tag{4.19}$$

an integral operator representative of the fluid inertia and

$$K[y; Bo] \equiv -Bo\, y + \left[\frac{\mathrm{d}^2}{\mathrm{d}r^2} + \frac{1}{r}\frac{\mathrm{d}}{\mathrm{d}r} - \frac{\ell^2}{r^2}\right] y, \tag{4.20}$$

a differential operator representative of the restorative forces of surface tension and gravity.

4.5. *Rayleigh–Ritz method*

An approximate solution to the eigenvalue problem (4.18) is constructed using the Rayleigh–Ritz method, where the pinned contact-line condition $y|_{r=1} = 0$ and volume conservation condition (4.12) are built into the function space over which the minimization is done. This approach has been applied previously to constrained drops by Bostwick & Steen (2009, 2013*a*,*b*).

We begin by defining a set of functions that satisfy the pinned edge condition,

$$S_n^\ell(r) = \mathrm{J}_\ell(k_{n\ell} r) - \frac{\mathrm{J}_\ell(k_{n\ell})}{\mathrm{J}_\ell(k_{1\ell})}\mathrm{J}_\ell(k_{1\ell} r), \quad n = 2, 3, \ldots, N. \tag{4.21}$$

Note the summation starts at $n = 2$. It is straightforward to show that the integral constraint (4.12) for $\ell = 0$ is naturally satisfied for this choice of basis functions by using the Bessel function identity $\int_0^1 r\mathrm{J}_0(kr)\,\mathrm{d}r = -\mathrm{J}_0'(k)/k^2$. Since k_{n0} was chosen such that $\mathrm{J}_0'(k) = 0$, it follows that $\int_0^1 r\mathrm{J}_0(k_{n0}r)\,\mathrm{d}r = 0$ and using linearity gives $\int_0^1 rS_n^0(r)\,\mathrm{d}r = 0$ for all n. The functions S_n^ℓ are not orthogonal, but the Gram–Schmidt procedure can be applied to generate a set of orthonormal basis functions $V_i^\ell(r)$, where $i = 1, 2, 3, \ldots, N$, such that $\int_0^1 rV_i^\ell(r)V_j^\ell(r)\,\mathrm{d}r = \delta_{ij}$ with δ_{ij} the Kronecker delta function. The surface disturbance y can be re-expressed using this orthonormal set as

$$y(r) = \sum_{i=1}^{\infty} c_i V_i^\ell(r). \tag{4.22}$$

Equation (4.22) is applied to the operator (4.18) and inner products are taken to yield the matrix equation

$$(\lambda^2 \boldsymbol{M} + \boldsymbol{K})\boldsymbol{c} = 0, \tag{4.23}$$

with matrices $\boldsymbol{M}$ and $\boldsymbol{K}$ defined as

$$\boldsymbol{M} = \left\langle M[V_i], V_j \right\rangle, \quad \boldsymbol{K} = \left\langle K[V_i], V_j \right\rangle, \tag{4.24a,b}$$

and $\boldsymbol{c}$ the coefficient vector.

4.6. *Results*

Equation (4.23) is a standard matrix eigenvalue problem that can be solved numerically using the MATLAB function polyeig for the eigenvalue/vector pairs $(\lambda, \boldsymbol{c})$. For the results presented here, we use a truncation of $N = 30$ which produces relative eigenvalue convergence of 0.01 %. The convergence properties of eigenvalues and eigenvectors using the Rayleigh–Ritz method are discussed in Segel (1987).

Each eigenvalue $\lambda_{n,\ell}$ and eigenvector $\boldsymbol{c}_{n,\ell}$ pair can be distinguished by the mode number pair (n, ℓ), where n and ℓ are the radial and azimuthal mode numbers, respectively. Figure 11 illustrates the modal structure through the (*a–c*) interface deflection and (*d–f*) one minus the absolute value of the wave slope, of which the latter can be compared directly to our experimental imaging technique. With regard to the interface deflection for a given mode (n, ℓ), the azimuthal wavenumber ℓ represents the number of polar sectors, whereas the radial mode number n represents the number of nodes, or locations of zero displacement, in the radial direction. For example, the (1, 2) mode has $\ell = 2$ sectors illustrated by the two lobes and $n = 1$ radial node. In the one minus the absolute value of wave slope rendering, the azimuthal mode number ℓ is represented by the 2ℓ dark sectors

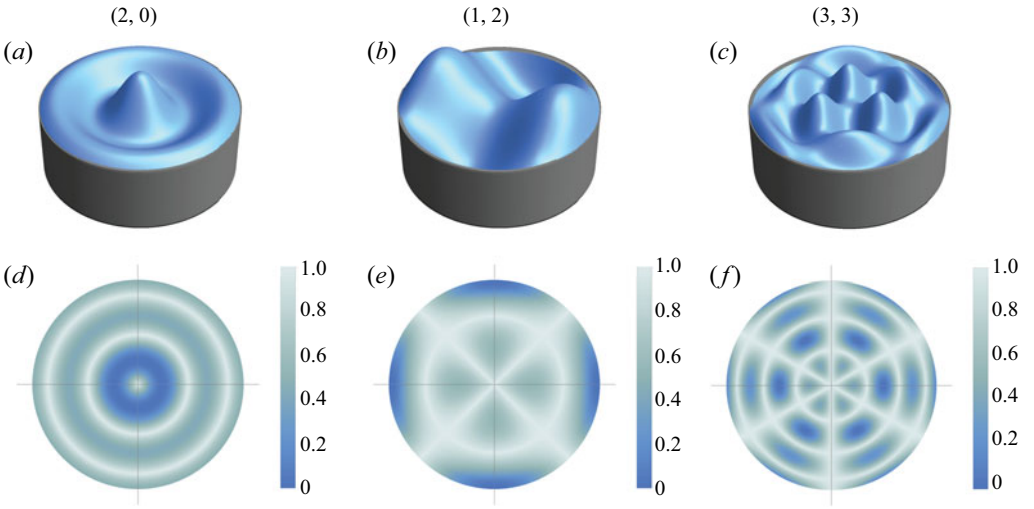

Figure 11. Mode (n, ℓ) predictions plotting surface shape (*a–c*) and one minus absolute value of wave slope (*d–f*).

emanating from the origin and the radial mode number n by the number of radial minima, which appear as dark rings in figure 11; e.g. the $(1, 2)$ mode has $2\ell = 4$ rays and $n = 1$ radial minima (dark ring). Note the outermost dark ring is due to the pinned meniscus and is not included in the counting. We have used these predictions to identify modal structure in experiment by performing 2-D cross-correlations with the absolute value of wave slope. For a given experimental mode, a table of 2-D cross-correlations can be computed and the maximum value used to identify the mode number pair (n, ℓ). This was done for the table of modes shown in figure 5 and the modal structure was unambiguous.

The discrete spectrum for λ varies with the set of parameters (h, Bo). Figure 12 plots the frequency λ against aspect ratio h for the Bond number $Bo = 167$ used in our experiments. For each mode (n, ℓ), the frequency increases with h and then plateaus. This is the infinite depth limit and we note this transition happens at different aspect ratios for each mode. This transition shifts to lower h for increasing frequency and this indicates the fluid motion becomes more localized to the surface for these modes. The lowest frequency $(1, 1)$ sloshing mode is most affected by the container depth. We note that the $(2, 0)$ and $(1, 5)$ modes have nearly the same frequency and this is most likely the reason that we could not experimentally observe an instability tongue for either of these modes in the frequency sweep shown in figure 4.

Figure 13 is a plot of the frequency λ against Bond number Bo for the aspect ratio $h = 0.628$ used in our experiments and shows a monotonically increasing trend with Bo for each mode. Pure capillary waves occur in regions where the curve is flat and capillary–gravity waves in regions where the curve is steadily increasing. The transition from capillary waves to capillary–gravity waves occurs at critical Bond number Bo which increases with frequency and mode number, as could be expected.

4.7. *Comparison to experiment*

We can compare our theoretical predictions with the experimental observations shown in figure 5 with the understanding that the response is sub-harmonic $f_o = 0.5 f_d$. That is, to excite a Faraday wave in experiment requires one to use a driving frequency twice

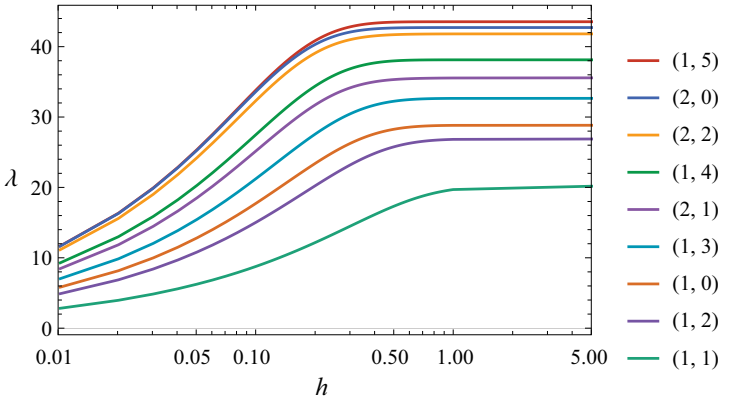

Figure 12. Frequency λ against aspect ratio h for $Bo = 167$.

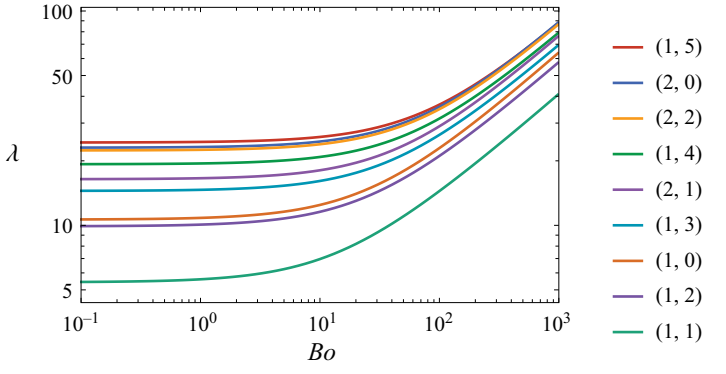

Figure 13. Frequency λ against Bond number Bo for $h = 0.628$.

the natural frequency for a given mode. Table 1 lists the computed natural frequencies for the modes (n, ℓ) observed in experiment. The agreement is excellent with nearly all predictions within 1 % of the experimental values. We note that these small per cent errors are somewhat fortuitous given that the 0.2 Hz spacing in driving frequency used in searching for resonance in the experiments gives an uncertainty in the experimentally determined resonance frequency that is larger than the stated errors for most entries in table 1. The comparison with the harmonic edge waves shown in figure 6 is also excellent when we associate the resonance peaks with the corresponding natural frequencies. Lastly, we note the comparison between theory and experiments by Henderson & Miles (1994) shows similarly good agreement for a different set of experimental conditions, as shown in table 2.

5. Concluding remarks

We have studied pattern formation on mechanically excited surface waves with a controlled meniscus geometry in a cylindrical container from both experimental and theoretical perspectives. The container geometry dictates the symmetry of the surface waves which are described by the integer-valued mode number pair (n, ℓ). The wave dynamics can be complex and this is controlled by the experimental conditions through the (i) driving amplitude and (ii) control of the contact angle at the lateral boundary of the container by

	$n=1$	2	3	4	5	6
$\ell=0$	5.82 (0.4 %)	8.67 (0.3 %)	11.68 (0.2 %)	15.05 (1.0 %)	18.80 (1.1 %)	22.92 (0.8 %)
1	3.71 (0.2 %)	7.20 (0.0 %)	10.10 (0.0 %)	13.29 (0.1 %)	16.85 (0.3 %)	20.79 (0.5 %)
2	5.33 (0.5 %)	8.47 (0.3 %)	11.53 (0.3 %)	14.92 (0.1 %)	18.68 (0.6 %)	22.81 (0.8 %)
3	6.58 (0.4 %)	9.73 (0.7 %)	12.98 (0.1 %)	16.58 (0.7 %)	20.54 (0.3 %)	—
4	7.71 (0.1 %)	11.00 (0.0 %)	14.47 (0.5 %)	18.28 (0.4 %)	—	—
5	8.81 (1.0 %)	12.30 (0.8 %)	15.99 (0.7 %)	20.01 (0.9 %)	—	—
6	9.93 (0.3 %)	13.64 (1.0 %)	17.56 (0.8 %)	21.78 (0.5 %)	—	—
7	11.06 (1.2 %)	15.02 (0.5 %)	19.16 (0.2 %)	—	—	—
8	12.23 (0.6 %)	16.43 (0.4 %)	—	—	—	—
9	13.43 (0.3 %)	17.89 (3.9 %)	—	—	—	—
10	14.68 (0.8 %)	19.39 (2.6 %)	—	—	—	—
11	15.96 (0.3 %)	20.92 (1.3 %)	—	—	—	—
12	17.28 (0.1 %)	—	—	—	—	—
13	18.64 (0.3 %)	—	—	—	—	—
14	20.04 (0.7 %)	—	—	—	—	—
15	21.49 (0.1 %)	—	—	—	—	—

Table 1. Theoretical natural frequency predictions measured in Hz for modes (n, ℓ) with comparison against experimental observation for $Bo = 167$ and $h = 0.628$.

H&M 94	Predictions			
(s, m)	f (Hz)	(n, ℓ)	f (Hz)	% difference
(1, 0)	4.65	(1, 1)	4.71	1.4 %
(2, 0)	6.32	(1, 2)	6.41	1.4 %
(0, 1)	6.84	(1, 0)	6.89	0.7 %
(3, 0)	7.80	(1, 3)	7.90	1.3 %
(4, 0)	9.26	(1, 4)	9.37	1.2 %
(1, 1)	8.57	(2, 1)	8.65	1.0 %

Table 2. Theoretical frequency predictions measured in Hz for modes (n, ℓ) with comparison against Henderson & Miles (1994) experiments for $Bo = 99.3$ and $h = 1.37$. Note the different modal classification systems, (s, m) and (n, ℓ).

under-filling or over-filling the tank whose interface is pinned at the rim. For $\alpha = 90^\circ$, the air/water interface remains flat until a threshold driving amplitude is reached coinciding with the emergence of a sub-harmonic Faraday wave pattern and we have experimentally observed the first 50 resonant modes (cf. figure 5). The situation is different when the container is under-filled, creating a concave meniscus in which case we observe (i) harmonic edge waves with $\ell = 0$ for driving amplitudes below the Faraday wave threshold (figure 6) and (ii) the simultaneous excitation of a harmonic edge wave and sub-harmonic Faraday wave above the threshold, which creates a complex, beautiful surface pattern (cf. figure 9). Theoretical predictions for the natural frequencies of an inviscid liquid in a cylindrical container with a pinned contact line are generated using the Rayleigh–Ritz procedure over a constrained function space and show excellent agreement with experiment.

Our experimental technique contrasts with those in the literature in that we purposefully create a pinned meniscus and control its geometry to suppress edge waves in order to study the onset of pure Faraday waves. Other authors have used either (i) large aspect ratio containers to minimize the effect of edge waves or (ii) surfactants to create a sliding edge condition which also suppresses edge waves. Our technique allows us to cleanly define

the instability tongues for a large number of modes (cf. figure 4). Furthermore, our optical technique that includes generating long exposure time images that are processed using 2-D cross-correlations to identify the modal structure is both inexpensive and efficient. These techniques could be applied to other interfacial pattern formation phenomena. Among the more interesting experimental observations is that we have shown by controlling the meniscus geometry, surface waves can be excited with a complex dynamics that includes the mixing of two unique spatial modes at the same driving frequency; one harmonic edge wave and one sub-harmonic Faraday wave (cf. figures 8 and 9). This system could be further exploited to explore nonlinear wave interactions.

For a perfectly flat interface, there is a discrete spectrum of resonance frequencies and mode shapes for which our theoretical predictions show excellent agreement with experimental observations. The frequency spectrum can shift due to dissipation (or damping), either from finite viscosity or dynamic wetting effects, and this depends upon the dissipation generated by the respective mode (n, ℓ). It is well known that higher mode number shapes have more viscous dissipation, whereas the lower mode number shapes display more contact-line dissipation. Given that it is common for two distinct modes to have nearly the same resonance frequency (cf. figures 4 and 5), it could be expected that the order in which modes appear in a frequency sweep (i.e. spectral ordering) could change with increased dissipative effects. In addition, under-filling or over-filling of the container breaks the symmetry of the flat interface by creating a meniscus with a given contact angle. This geometric wetting effect has been shown to shift the resonance frequency for sessile drops such that the spectrum reorders (Bostwick & Steen 2014; Chang *et al.* 2015). For this case, a new organizing principle has been developed that culminates in the periodic table of droplet motions (Steen, Chang & Bostwick 2019). By exploiting our experimental approach to include a range of contact angles (as opposed to just the two explored herein), it may be possible to observe similar spectral reordering due to wetting effects and this should be explored further.

Funding. J.B.B. acknowledges support from NSF Grant CMMI-1935590.

Declaration of interests. The authors report no conflict of interest.

Author ORCIDs.
J.B. Bostwick https://orcid.org/0000-0001-7573-2108.

References

Batson, W., Zoueshtiagh, F. & Narayanan, R. 2013 The Faraday threshold in small cylinders and the sidewall non-ideality. *J. Fluid Mech.* **729**, 496–523.

Batson, W., Zoueshtiagh, F. & Narayanan, R. 2015 Two-frequency excitation of single-mode Faraday waves. *J. Fluid Mech.* **764**, 538–571.

Bechhoefer, J., Ego, V., Manneville, S. & Johnson, B. 1995 An experimental study of the onset of parametrically pumped surface waves in viscous fluids. *J. Fluid Mech.* **288**, 325–350.

Benjamin, T.B. & Scott, J.C. 1979 Gravity-capillary waves with edge constraints. *J. Fluid Mech.* **92** (2), 241–267.

Benjamin, T.B. & Ursell, F.J. 1954 The stability of the plane free surface of a liquid in vertical periodic motion. *Proc. R. Soc. Lond.* A **225** (1163), 505–515.

Bostwick, J.B. & Steen, P.H. 2009 Capillary oscillations of a constrained liquid drop. *Phys. Fluids* **21**, 032108.

Bostwick, J.B. & Steen, P.H. 2013*a* Coupled oscillations of deformable spherical-cap droplets. Part 1. Inviscid motions. *J. Fluid Mech.* **714**, 312–335.

Bostwick, J.B. & Steen, P.H. 2013*b* Coupled oscillations of deformable spherical-cap droplets. Part 2. Viscous motions. *J. Fluid Mech.* **714**, 336–360.

BOSTWICK, J.B. & STEEN, P.H. 2014 Dynamics of sessile drops. Part 1. Inviscid theory. *J. Fluid Mech.* **760**, 5–38.
BOSTWICK, J.B. & STEEN, P.H. 2015 Stability of constrained capillary surfaces. *Annu. Rev. Fluid Mech.* **47**, 539–568.
BOSTWICK, J.B. & STEEN, P.H. 2016 Response of driven sessile drops with contact-line dissipation. *Soft Matt.* **12** (43), 8919–8926.
BRIARD, A., GOSTIAUX, L. & GRÉA, B.-J. 2020 The turbulent Faraday instability in miscible fluids. *J. Fluid Mech.* **883**, A57.
CHANG, C.-T., BOSTWICK, J.B., DANIEL, S. & STEEN, P.H. 2015 Dynamics of sessile drops. Part 2. Experiment. *J. Fluid Mech.* **768**, 442–467.
CHEN, P., GÜVEN, S., USTA, O.B., YARMUSH, M.L. & DEMIRCI, U. 2015 Biotunable acoustic node assembly of organoids. *Adv. Healthc. Mater.* **4** (13), 1937–1943.
CHEN, P., LUO, Z., GÜVEN, S., TASOGLU, S., GANESAN, A.V., WENG, A. & DEMIRCI, U. 2014 Microscale assembly directed by liquid-based template. *Adv. Mater.* **26** (34), 5936–5941.
CHRISTIANSEN, B., ALSTRØM, P. & LEVINSEN, M.T. 1995 Dissipation and ordering in capillary waves at high aspect ratios. *J. Fluid Mech.* **291**, 323–341.
CILIBERTO, S. & GOLLUB, J.P. 1985 Chaotic mode competition in parametrically forced surface waves. *J. Fluid Mech.* **158**, 381–398.
CILIBERTO, S. & GOLLUB, J.P. 1984 Pattern competition leads to chaos. *Phys. Rev. Lett.* **52** (11), 922.
DAVIS, S.H. 1980 Moving contact lines and rivulet instabilities. Part 1. The static rivulet. *J. Fluid Mech.* **98**, 225–242.
DOUADY, S. 1990 Experimental study of the Faraday instability. *J. Fluid Mech.* **221**, 383–409.
DOUADY, S. & FAUVE, S. 1988 Pattern selection in Faraday instability. *Europhys. Lett.* **6** (3), 221.
EDWARDS, W.S. & FAUVE, S. 1994 Patterns and quasi-patterns in the Faraday experiment. *J. Fluid Mech.* **278**, 123–148.
FARADAY, M. 1831 XVII. On a peculiar class of acoustical figures; and on certain forms assumed by groups of particles upon vibrating elastic surfaces. *Phil. Trans. R. Soc. Lond.* **121**, 299–340.
GHADIRI, M. & KRECHETNIKOV, R. 2019 Pattern formation on time-dependent domains. *J. Fluid Mech.* **880**, 136–179.
GLUCKMAN, B.J., MARCQ, P., BRIDGER, J. & GOLLUB, J.P. 1993 Time averaging of chaotic spatiotemporal wave patterns. *Phys. Rev. Lett.* **71** (13), 2034–2037.
GRAHAM-EAGLE, J. 1983 A new method for calculating eigenvalues with applications to gravity-capillary waves with edge constraints. In *Mathematical Proceedings of the Cambridge Philosophical Society*, vol. 94, pp. 553–564. Cambridge University Press.
GUVEN, S., CHEN, P., INCI, F., TASOGLU, S., ERKMEN, B. & DEMIRCI, U. 2015 Multiscale assembly for tissue engineering and regenerative medicine. *Trends Biotechnol.* **33** (5), 269–279.
HENDERSON, D.M. & MILES, J.W. 1990 Single-mode Faraday waves in small cylinders. *J. Fluid Mech.* **213**, 95–109.
HENDERSON, D.M. & MILES, J.W. 1991 Faraday waves in 2: 1 internal resonance. *J. Fluid Mech.* **222**, 449–470.
HENDERSON, D.M. & MILES, J.W. 1994 Surface-wave damping in a circular cylinder with a fixed contact line. *J. Fluid Mech.* **275**, 285–299.
HOCKING, L.M. 1987 The damping of capillary-gravity waves at a rigid boundary. *J. Fluid Mech.* **179**, 253–266.
JAMES, A., VUKASINOVIC, B., SMITH, M.K. & GLEZER, A. 2003 Vibration-induced drop atomization and bursting. *J. Fluid Mech.* **476**, 1–28.
KIM, J. 2007 Spray cooling heat transfer: the state of the art. *Intl J. Heat Fluid Flow* **28** (4), 753–767.
KUMAR, K. 1996 Linear theory of Faraday instability in viscous liquids. *Proc. R. Soc. Lond.* A **452** (1948), 1113–1126.
KUMAR, K. & TUCKERMAN, L.S. 1994 Parametric instability of the interface between two fluids. *J. Fluid Mech.* **279**, 49–68.
MARTEL, C., NICOLAS, J.A. & VEGA, J.M. 1998 Surface-wave damping in a brimful circular cylinder. *J. Fluid Mech.* **360**, 213–228.
MELO, F., UMBANHOWAR, P. & SWINNEY, H.L. 1994 Transition to parametric wave patterns in a vertically oscillated granular layer. *Phys. Rev. Lett.* **72** (1), 172–175.
MILES, J. & HENDERSON, D. 1990 Parametrically forced surface waves. *Annu. Rev. Fluid Mech.* **22** (1), 143–165.
MILES, J.W. & HENDERSON, D.M. 1998 A note on interior vs. boundary-layer damping of surface waves in a circular cylinder. *J. Fluid Mech.* **364**, 319–323.

MÜLLER, H.W., WITTMER, H., WAGNER, C., ALBERS, J. & KNORR, K. 1997 Analytic stability theory for Faraday waves and the observation of the harmonic surface response. *Phys. Rev. Lett.* **78** (12), 2357.

PERLIN, M. & SCHULTZ, W.W. 2000 Capillary effects on surface waves. *Annu. Rev. Fluid Mech.* **32** (1), 241–274.

PROSPERETTI, A. 2012 Linear oscillations of constrained drops, bubbles, and plane liquid surfaces. *Phys. Fluids* **24** (3), 032109.

SAYLOR, J.R. & KINARD, A.L. 2005 Simulation of particle deposition beneath Faraday waves in thin liquid films. *Phys. Fluids* **17** (4), 047106.

SEGEL, L.A. 1987 *Mathematics Applied to Continuum Mechanics*. Dover Publications.

STEEN, P.H., CHANG, C.-T. & BOSTWICK, J.B. 2019 Droplet motions fill a periodic table. *Proc. Natl Acad. Sci.* **116** (11), 4849–4854.

STRICKLAND, S.L., SHEARER, M. & DANIELS, K.E. 2015 Spatiotemporal measurement of surfactant distribution on gravity–capillary waves. *J. Fluid Mech.* **777**, 523–543.

TSAI, C.S., MAO, R.W., LIN, S.K., ZHU, Y. & TSAI, S.C. 2014 Faraday instability-based micro droplet ejection for inhalation drug delivery. *Technology* **2** (01), 75–81.

VUKASINOVIC, B., SMITH, M.K. & GLEZER, A. 2007 Dynamics of a sessile drop in forced vibration. *J. Fluid Mech.* **587**, 395–423.

WARD, K., ZOUESHTIAGH, F. & NARAYANAN, R. 2019 Faraday instability in double-interface fluid layers. *Phys. Rev. Fluids* **4** (4), 043903.

WRIGHT, P.H. & SAYLOR, J.R. 2003 Patterning of particulate films using Faraday waves. *Rev. Sci. Instrum.* **74** (9), 4063–4070.